

Turing instability under centrifugal forces

Cite this: *Soft Matter*, 2013, 9, 4509Jacobó Guíu-Souto,^{*a} Lisa Michaels,^b Alexandra von Kameke,^a Jorge Carballido-Landeirot^a and Alberto P. Muñozuri^a

Self-organized patterns are sensitive to microscopic external perturbations that modify the diffusion process. We find that Turing instability formed in a compartmented medium, a Belousov–Zhabotinski–aerosol-OT micelle reaction, responds sensitively to a change in the diffusion process. In order to modify the diffusion mechanism, we apply a centrifugal force that generates a perturbation with an anisotropic character. We find experimentally and numerically that the perturbation is able to modify the pattern and even force its disappearance. For different values of the perturbation significant changes can be seen in both the pattern wavelength and its morphology. Furthermore, for strong perturbations, the orientation of the patterns couples with the symmetry of the perturbation.

Received 14th November 2012
Accepted 22nd February 2013

DOI: 10.1039/c3sm27624d

www.rsc.org/softmatter

Introduction

Self-organization is a characteristic of many living systems that involves three fundamental properties: order, pattern and form.¹ Thereby the involved physico-chemical mechanisms allow these systems to evolve from an initially disordered stage into a pattern-organized configuration with well-defined macroscopic properties. In the last few decades, this phenomenon has been studied from a theoretical point of view^{2,3} concluding that many nonlinear systems can lead to macroscopic self-organization.

One of the most important mechanisms capable of generating organization through pattern formation is the Turing instability in reaction–diffusion systems.^{4,5} It is thought to be responsible for morphogenesis^{6,7} in living organisms, for example, patterning on the fish skin⁸ or seashells.⁹ In Nature, pattern formation does not occur in isolated systems but usually in the presence of different external perturbations, as for example, changes in the temperature, density gradients,^{10–12} and even certain types of periodical forces such as modulated gravity or differential flows.^{13–15} Furthermore, pattern formation in the presence of a centrifugal force has been studied in different systems such as Rayleigh–Bénard cells or active media.^{16–18}

Here we considered the Belousov–Zhabotinsky reaction^{19,20} encapsulated into AOT micelles¹⁹ (BZ–AOT system). Experimentally, this system is shown to exhibit Turing patterns for the appropriate concentrations of the reactants. We impose a centrifugal force in such a way that any fluid flow is suppressed, and the only transport process is the microscopic diffusion of

micelles and reactants due to the physical constraints of the system. The experimental observations are explained by theoretical analysis. Furthermore, numerical simulations confirm and complement the experiments.

Methods

Experimental description

Two stock microemulsions (MEs), ME₁ and ME₂, with the same molar ratio, $w = [\text{H}_2\text{O}]/[\text{AOT}] (=18)$, and the same droplet volume fraction, $\Phi_d (=0.72)$, were prepared at room temperature by mixing aqueous solutions of Belousov–Zhabotinsky (BZ) reactants and an oily 1.5 M solution of aerosol-OT (ref. 21) in octane. ME₁ was composed of solutions of malonic acid (0.5 M) and sulphuric acid (0.3 M), while for ME₂ we used bromate (0.32 M) and ferroin (8.3 mM) as described in ref. 22. The reactive microemulsion, BZ–AOT reaction system,^{23–25} was obtained by mixing equal volumes of the two MEs and diluting the mixture with octane to the desired droplet fraction ($\Phi_d = 0.48$).

The behaviour of the reaction is governed by the two main species, also known as the activator (bromous acid) and the inhibitor (bromine) due to their chemical competition processes.²³ The activator molecules remain on the inside of the AOT-micelles in the aqueous phase, due to their polar nature and ionic dissociation, and only the non-polar molecules (inhibitor) can go through the micelle membrane and move into the oil phase. The polar compound, the activator, is confined to the aqueous phase within the micelle and its diffusion is linked to that of the micelle. Thus, in the following, we will consider the activator mass as that of the micelle containing it. The micelle mass can be estimated²² given the hydrodynamic radius of our micelles²³ ($R \sim 1$ nm) and we obtain a value of 2500 amu. As a conclusion, the activator diffusion coefficient is much smaller than the inhibitor diffusion coefficient (approximately, 10^{-9} m² s⁻¹ and 10^{-7} m² s⁻¹, respectively²³).

^aGroup of Nonlinear Physics, Universidade de Santiago de Compostela, E-15782 Santiago de Compostela, Spain. E-mail: jacobó.guíu@usc.es

^bMax-Planck-Institut fuer Kernphysik, Saupfercheckweg 1, 69117 Heidelberg, Germany

† Present address: Planetary Sciences, Harvard University, 100 Edwin H. Land Boulevard Cambridge, MA 02142-1204

A small amount of the reactive ME was sandwiched between two optical glasses separated by a Teflon gasket (thickness 80 μm , inner diameter 25 mm, and outer diameter 50 mm, see Fig. 1). This reactor was placed at different distances, R , from 0 up to 20 cm from the rotation center of the rotor (Geared Brushless 24V DC), performing an uniform circular motion on the horizontal plane, with a maximum peak angular velocity of $\omega = 40 \text{ rad s}^{-1}$. The system is such that no convective flow may occur and this will be discussed below.

The rotating BZ-AOT system was analyzed with the following acquisition image set. In order to achieve optimal contrast, the sample was illuminated with a blue high-intensity diode array LED. The light passes through a series of light diffusers until reaching the reactor in order to guarantee uniform background illumination. The image of the reactor was magnified with an achromatic objective (DIN 4 \times Edmund Optics), recorded by a camera (Guppy AVT 64 fps) and was finally processed in the computer. In order to quantify the effect of the rotational force, we compare the differences between two identical reaction samples. One of them is subjected to a rotational motion and the other is left at rest, it is subsequently referred to as the standard pattern. This procedure is repeated for different angular velocities and radii, obtaining a range of force from $\omega R = 0 \text{ m s}^{-1}$ to $\omega R = 8 \text{ m s}^{-1}$. The required time for the pattern to appear and its evolution into the steady state is ~ 40 min. The room temperature was kept constant at $20 \pm 2 \text{ }^\circ\text{C}$. All experiments lying on the same iso-velocity line ($v = \omega R$) exhibit the same behaviour and thus can be averaged for statistical purposes.

BZ-AOT numerical model

The kinetics of the BZ-AOT reaction can be modelled by the Oregonator equations revised in ref. 26:

$$F_1 = \frac{dc_1}{dt} = \frac{1}{\varepsilon} \left(fc_2 \frac{q - c_1}{q + c_1} + c_1 \frac{1 - mc_2}{1 - mc_2 + \varepsilon_1} - c_1^2 \right) \quad (1)$$

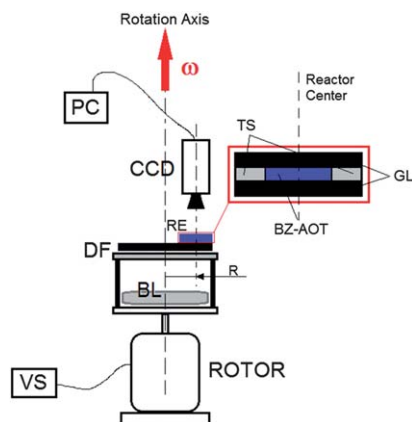


Fig. 1 Experimental setup. The rotor is controlled by a voltage source (VS) that generates a uniform angular velocity ω . BL is the blue LED array used for illumination and DF is the diffuser. The CCD camera on top of the reactor center is connected to a PC. The reactor (RE), where the BZ-AOT reaction takes place, is composed of a Teflon separator (TS) and two optical glasses (GL). R is the distance from the rotation axis to the reactor center.

$$F_2 = \frac{dc_2}{dt} = c_1 \frac{1 - mc_2}{1 - mc_2 + \varepsilon_1} - c_1 \quad (2)$$

where the subindex $i = 1, 2$ labels the activator and inhibitor species, and c_i are their respective dimensionless concentrations. The parameters f, m, q, ε_1 and ε depend on the reaction rates and they appear as a result of applying the mass action law on the chemical equations.²⁷ The suitable values to model the BZ-AOT system²⁸ are $f = 1.2, m = 190, q = 0.001, \varepsilon_1 = 0.01$ and $\varepsilon = 0.8$, as used throughout this study. Numerical simulations of eqn (7) are performed by applying an explicit three-level Du Fort–Frankel scheme²⁹ with a spatial step of 0.2 s.u. and zero flux boundary conditions. To trigger instability we use random noise as an initial condition.

Experimental results

Fig. 2a shows experimental results in the absence of force. Turing patterns appear as a mixed state that is composed of stripes and spots with a labyrinthine configuration. However, when we increase the force to 4.7 m s^{-1} (Fig. 2b) two different phenomena can be distinguished: the dominance of stripes over spots and the soft orientation of patterns along the direction of the centripetal force. Higher force values intensify these phenomena and stripe-like patterns completely orient along the direction of the force (Fig. 2c). The phase diagram can be divided into three representative regions, as shown in Fig. 2g.

The first region, from $\omega R = 0 \text{ m s}^{-1}$ up to $\omega R = 2 \text{ m s}^{-1}$, is characterized by patterns that maintain a mixed configuration (labyrinth patterns). The second region corresponds to ωR values ranging from 2 m s^{-1} up to 5 m s^{-1} (see discussion of Fig. 6). Here, the system exhibits an intermediate state where the orientation phenomenon begins to occur (transition stage). Finally above 5 m s^{-1} all patterns present are well-oriented stripes in the direction given by the centrifugal force (oriented patterns).

Moreover, the pattern wavelength augments slightly according to the centrifugal force as will be discussed below (Fig. 5). It is interesting to note that the organization mechanisms studied here are similar to those studied for fish skin pattern formation by using the CDIMA reaction–diffusion model,³⁰ where the velocity of a growing boundary determines the final structure of the pattern.

Theoretical approach

In order to understand the phenomena induced by a centrifugal force, we propose a theoretical model based on a statistical mechanics approach. The characteristics of our encapsulated reactor allow us to neglect any macroscopic flow,²² and therefore, the only transport mechanism is due to molecular diffusion.^{31,32} This approximation is possible because the thickness (80 μm) of our system is much smaller than the estimated boundary layer thickness³³ (~ 3 cm). Given that no convective transport may exist in this system, the only effect of the external force is an alteration of the diffusion mechanism. According to

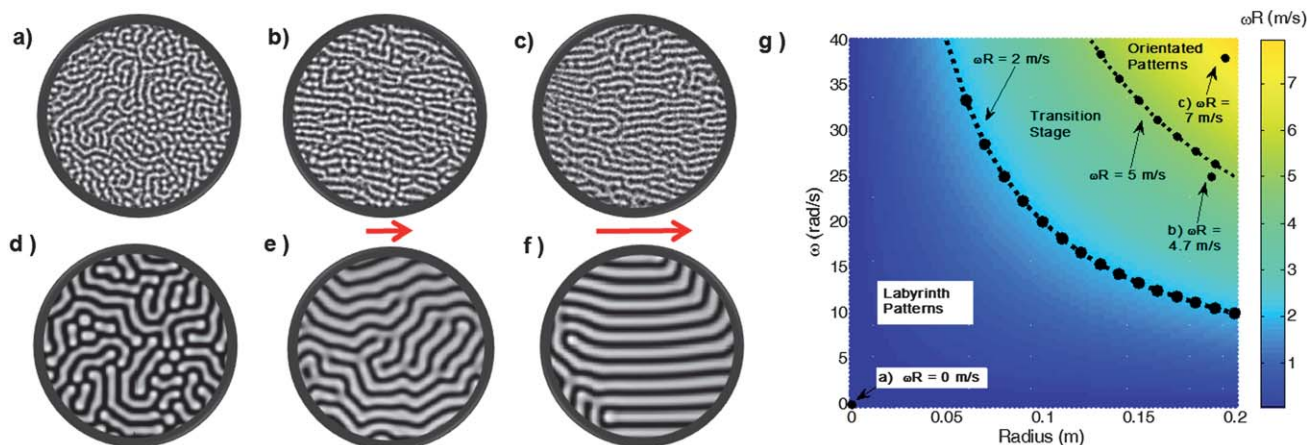


Fig. 2 Turing pattern under centrifugal force (direction represented by the red arrow) far from the rotation center. The patterns orient in the direction of the force. Experimental (top row) and numerical (bottom row) Turing patterns obtained at different force values: (a and d) $\omega R = 0 \text{ m s}^{-1}$, (b and e) $\omega R = 4.7 \text{ m s}^{-1}$ and (c and f) $\omega R = 7 \text{ m s}^{-1}$. The experimental images have a radius of 1.53 mm and the computational domain consists of a two-dimensional mesh of 300×300 grid points, with a spatial step of 0.2 s.u.; (g) is the experimental (ω, R) -phase diagram with the corresponding characteristic velocities ωR . The iso-velocity curves $\omega R = 2 \text{ m s}^{-1}$ and $\omega R = 5 \text{ m s}^{-1}$ divide the diagram into three regions; labyrinth patterns, transition stage and oriented patterns.

this, canonical ensemble considerations can be applied in order to evaluate the influence of the force on the microscopic diffusion processes.³⁴

We establish an expression for the position of the activator and the inhibitor inside of the reactor by coupling the thermal fluctuations with the rotational motion:

$$r_i = x_i \hat{x} + y_i \hat{y} + z_i \hat{z} = (x'_i + x_{\text{rot}}) \hat{x} + (y'_i + y_{\text{rot}}) \hat{y} + z'_i \hat{z} \quad (3)$$

where $x_{\text{rot}} = R \cos(\omega t)$, $y_{\text{rot}} = R \sin(\omega t)$ and the subindex $i = 1, 2$ represents the activator and inhibitor species, respectively. The coordinates (x'_i, y'_i, z'_i) indicate the position of the particles due to thermal motion. Thus the resulting Hamiltonian associated with the kinetic contribution is:

$$H_i = \frac{p_i^2}{2m_i} + \frac{1}{2} m_i \omega^2 R^2 + \omega (p'_{y,i} x_{\text{rot}} - p'_{x,i} y_{\text{rot}}) \quad (4)$$

where $p_i = (p'_{x,i}, p'_{y,i}, p'_{z,i})$ and m_i denote the momentum and the masses of the particles. The first and the second term of the Hamiltonian represent the kinetic and rotational energy, respectively. The last term represents the angular momentum of the particles and it accounts for the coupling between the rotational motion and thermal fluctuations.

In order to estimate the changes in the diffusion processes due to the applied force, we consider a diluted system approximation³⁴ and assume that the microscopic collisions occur only between identical particles, *i.e.* 1–1 or 2–2. The 1–2 collisions are considered negligible because in the BZ–AOT reaction the inhibitor molecules can diffuse through the micelle membrane due their non-polar character.²³ One can also estimate easily the frequency of collisions and the results indicate that collisions of type 2–2 occur 100 times more frequently than those of type 1–1. All of these arguments allow us to consider each species independently.

Under these considerations we obtain the following expression for the diffusion coefficient of each species:^{31,34}

$$D_{1,2}(\beta, m_{1,2}, \omega, R) = \frac{D_{1,2}^0(\beta, m_{1,2})}{3\sqrt{3}} [3 + \beta m_{1,2} v^2]^{3/2} \quad (5)$$

$$D_{1,2}^0(\beta, m_{1,2}) = \frac{1}{8N\sigma_{\text{tot}}} \sqrt{\frac{3}{\beta m_{1,2}}} \quad (6)$$

where $v = \omega R$ is the characteristic force velocity, N is the volumetric density of the particles, σ_{tot} is the total collision cross-section, $D_{1,2}^0(\beta, m_{1,2})$ is the diffusion coefficient in the absence of force and $\beta = 1/k_B T$. This analytical expression, eqn (5), was obtained by considering that $\beta m_{1,2} \omega^2 R^2 \ll 1$ which is in agreement with the experimental conditions. For example, for the activator $\beta m_1 \omega^2 R^2 \sim 0.095$ at the experimental force threshold. It is also important to note that in the absence of force, *i.e.* $\omega R = 0 \text{ m s}^{-1}$, we recover the expressions for free diffusion.³⁴

In accordance with eqn (5) the diffusion process is anisotropic, since it depends on the direction and magnitude of the centrifugal force. Moreover, as $x_{\text{rot}}, y_{\text{rot}} \gg x', y'$, we consider the following approximations $x \sim x_{\text{rot}}$ and $y \sim y_{\text{rot}}$. Taking into account all these considerations the resulting reaction–diffusion equation for our rotating system is:

$$\frac{\partial c_i}{\partial t} = F_i + 2D_i^0 \beta m_i \omega^2 \sqrt{1 + \frac{1}{3} \Phi_i(x, y)} \left(x \frac{\partial c_i}{\partial x} + y \frac{\partial c_i}{\partial y} \right) + \frac{D_i^0}{3\sqrt{3}} (3 + \Phi_i(x, y))^{3/2} \left(\frac{\partial^2 c_i}{\partial x^2} + \frac{\partial^2 c_i}{\partial y^2} \right) \quad (7)$$

where c_i with $i = 1, 2$ represents the activator and inhibitor species, respectively. $\Phi_i(x, y) = \beta m_i \omega^2 (x^2 + y^2)$ is related to the magnitude of the centrifugal forces. F_i is the reaction term from eqn (1) and (2). The second term on the right corresponds to a microscopic flow obtained from $\nabla D_i \nabla c_i$. Finally, the last term represents the diffusive transport given by $D_i \nabla^2 c_i$.

By performing a linear stability analysis⁷ of eqn (7), we find the following eigenvalues Λ_{\pm} :

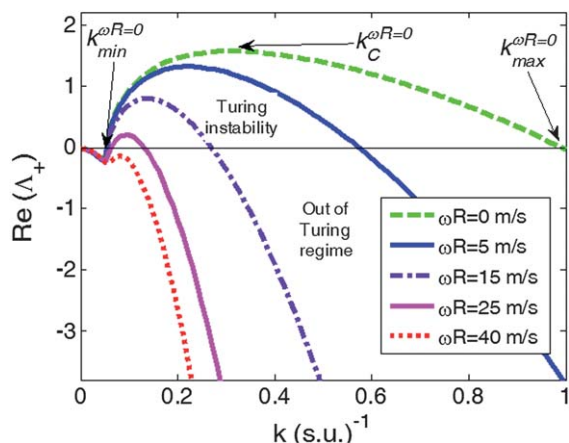


Fig. 3 The real part of the eigenvalues obtained by a linear stability analysis of eqn (7). The curves were calculated for the following values of force $\omega R = 0, 5, 15, 25$ and 40 m s^{-1} . The most probable Turing wavenumber k_C , is the maximum of each $\text{Re}(\lambda_+)$ curve and the Turing region (k_{\min}, k_{\max}) is given by the zero-crossing, i.e. $\text{Re}(\lambda_+(k_{\min, \max})) = 0$. For forces above $\omega R = 30 \text{ m s}^{-1}$ Turing patterns disappear.

$$2\lambda_{\pm} = -[k^2 \text{tr}(D) - jk \text{tr}(Z) - \text{tr}(J)] \pm \sqrt{[k^2 \text{tr}(D) - jk \text{tr}(Z) - \text{tr}(J)]^2 - 4\text{II}(k, D, J, Z)} \quad (8)$$

with,

$$\text{II}(k, D, J, Z) = k^4 \det(D) - jk^3 \text{tr}(D^*Z) - k^2 [\text{tr}(D^*J) + \det(Z)] + jk \text{tr}(JZ^*) + \det(J) \quad (9)$$

where k is the wavenumber, j the imaginary unit and J the Jacobian matrix corresponding to the linearization of the reaction terms, F_i . D is the diagonal diffusion matrix ($d_{ii} = D_i$), and Z is an auxiliary diagonal matrix ($z_{ii} = 3D_i^0 \beta m_i \omega(x + y)$) that

accounts for the anisotropy of the diffusion processes. The matrices D^* and Z^* are defined by $D^{-1} \det(D)$ and $Z^{-1} \det(Z)$, respectively. Once again, in the absence of force we recover the standard expressions for the reaction–diffusion system.³⁵

Fig. 3 shows the real eigenvalues, $\text{Re}(\lambda_+)$ versus the wavenumber for different forces. Positive values of $\text{Re}(\lambda_+)$ are responsible for generating the Turing instability. Negative values of the eigenvalue indicate the region where the Turing structures are unstable. Thus for each ωR -isovelocity-curve of Fig. 3 there are a range of wavenumbers denoted by (k_{\min}, k_{\max}) , where Turing patterns can be generated. Moreover, the most unstable wavenumber⁷ (k_C) inside that range determines the final observed stable configuration of the pattern, i.e. its critical wavelength given by the relationship $\lambda_C = 2\pi/k_C$. As the force is increased k_{\max} and k_C decrease and k_{\min} remains almost invariable. It points to the fact that the pattern wavelength, λ_C , increases with the force. Note that for values of the force above $\omega R = 30 \text{ m s}^{-1}$ Turing instability is inhibited.

Numerical results

Eqn (7) was numerically integrated and the results are shown in Fig. 2d–f. Note that they show a good agreement with the experimental observations; the radial force gradually orients the previously labyrinthine patterns in the direction of the centrifugal force. Additionally, we again obtain a structure that evolves from a mixed state composed of stripes and spots to a well-defined stripes configuration. Analogous to the experimental results, the numerical wavelength undergoes an increment that will be discussed in Fig. 5.

Fig. 4 shows the effect of a strong force close to the rotation center. In the absence of any force (Fig. 4a) we obtain a labyrinth-like pattern with a uniform wavelength and without a

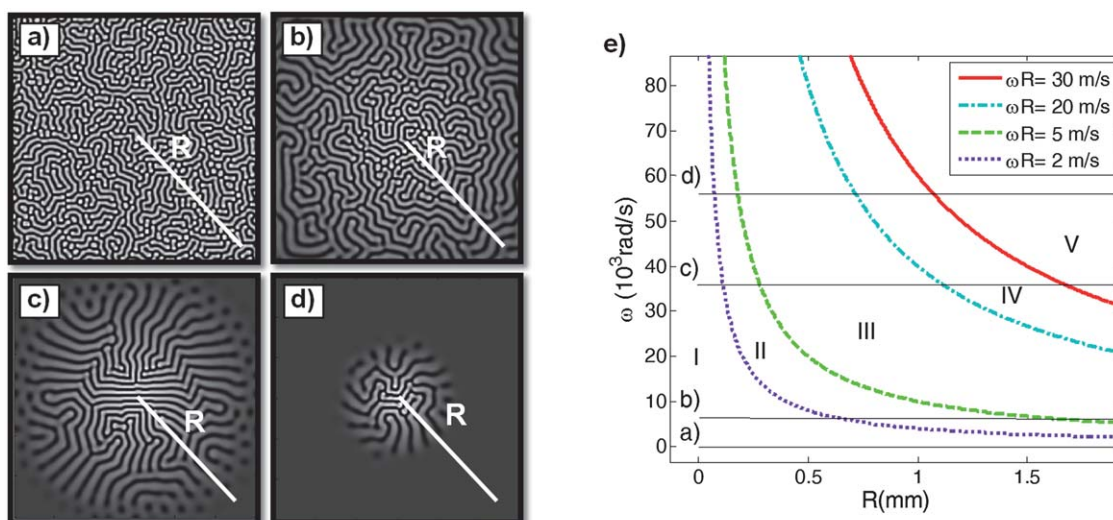


Fig. 4 Numerical study of Turing patterns under rotation. The center of rotation lies in the middle of the numerical domain. The radius scale is around the size of patterns (R ranges from 0 to 2 mm). (a) Labyrinth pattern in the absence of force. (b) Labyrinth pattern and transition stage at $\omega = 6 \times 10^3 \text{ rad s}^{-1}$. (c) Developed radial modifications (oriented stage and black spots), at $\omega = 35 \times 10^3 \text{ rad s}^{-1}$. (d) Pattern inhibition at $\omega = 57 \times 10^3 \text{ rad s}^{-1}$. A summary of all these results is plotted in the (ω, R) -phase diagram in (e). The iso-velocity curves $\omega R = 2 \text{ m s}^{-1}$, $\omega R = 5 \text{ m s}^{-1}$, $\omega R = 20 \text{ m s}^{-1}$ and $\omega R = 30 \text{ m s}^{-1}$ delimit five regions: I, II, III, IV and V related to the effects of force over the patterns. Lines (a) to (d) indicate the force situations of panel (a) to (d) on the left.

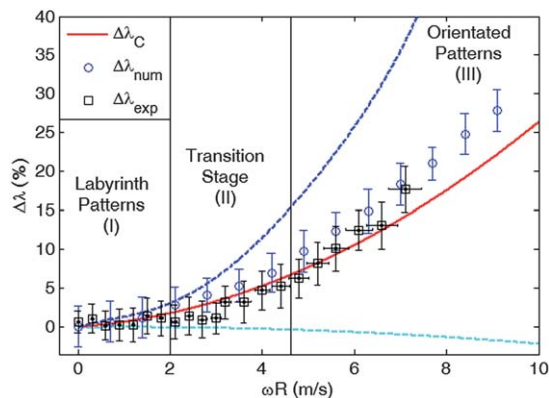


Fig. 5 Normalized wavelength ($\Delta\lambda = (\lambda - \lambda_0)/\lambda_0$, with λ_0 as the standard pattern wavelength) versus the force applied. The theoretical critical wavelength increment, $\Delta\lambda_C$ (red continuous line) from stability analysis, numerical estimations, $\Delta\lambda_{\text{num}}$ (blue circles), and experimental measures, $\Delta\lambda_{\text{exp}}$ (black squares) reflect a monotonous growth with the force. The theoretical region for Turing patterns lies between the maximum and the minimum wavelength increments, *i.e.* $\Delta\lambda_{\text{max}}$ and $\Delta\lambda_{\text{min}}$ (dashed lines). The uncertainties in the $\Delta\lambda$ were estimated from the width of the wavenumber ring obtained by a Fourier transform of the Turing patterns images. Uncertainties associated with ωR are estimated by the sensitivity of the experimental devices.

preferred direction. Similar to the experimental results, when we increase the angular velocity up to $\omega = 6 \times 10^3 \text{ rad s}^{-1}$, the pattern shows an increment in the wavelength with the radius, and also a growing dominance of stripes (Fig. 4b). At higher angular velocities, the patterns re-align along the direction of the force (see Fig. 4c and d) but also new phenomena are

observed. On the one hand, black spots appear at the boundary (see for example Fig. 4c), and on the other hand, for values higher than $\omega R = 30 \text{ m s}^{-1}$, Turing patterns are strongly inhibited (see Fig. 4d).

These different states are summarized in the numerical phase diagram shown in Fig. 4e. The iso-velocity curves ($\omega R = 2 \text{ m s}^{-1}$, $\omega R = 5 \text{ m s}^{-1}$, $\omega R = 20 \text{ m s}^{-1}$ and $\omega R = 30 \text{ m s}^{-1}$) divide the phase diagram into five regions denoted as I, II, III, IV and V. Region I includes the labyrinth patterns and region II the transition state shown in Fig. 2g. Region III corresponds to the experimental oriented regime. The black spots appear in region IV and the inhibition phenomenon occurs in region V. When this last region is reached the conditions for the Turing instability are not satisfied⁷ as we also observed from the analytical considerations. Lines marked with (a) to (d) in Fig. 4e show the values of R and ω in the corresponding Fig. 4a–d. Each one of these lines determines the transitions along the different regions (related to the type of pattern organization) in the phase diagram as seen in the corresponding Fig. 4a–d.

Discussion

Fig. 5 compares the differences in the wavelength of the Turing pattern for the experimental results, the numerical results and the theoretical predictions from Fig. 2 and 3. This comparison is feasible due to the dimensionless force term ($\beta m_{1,2} \omega^2 R^2$) and the use of the normalized wavelength increment, $\Delta\lambda$. This quantity is defined as $\Delta\lambda = (\lambda - \lambda_0)/\lambda_0$ where λ_0 stands for the wavelength of the pattern in the absence of external force, *i.e.*, the standard pattern. Note that the normalized wavelength

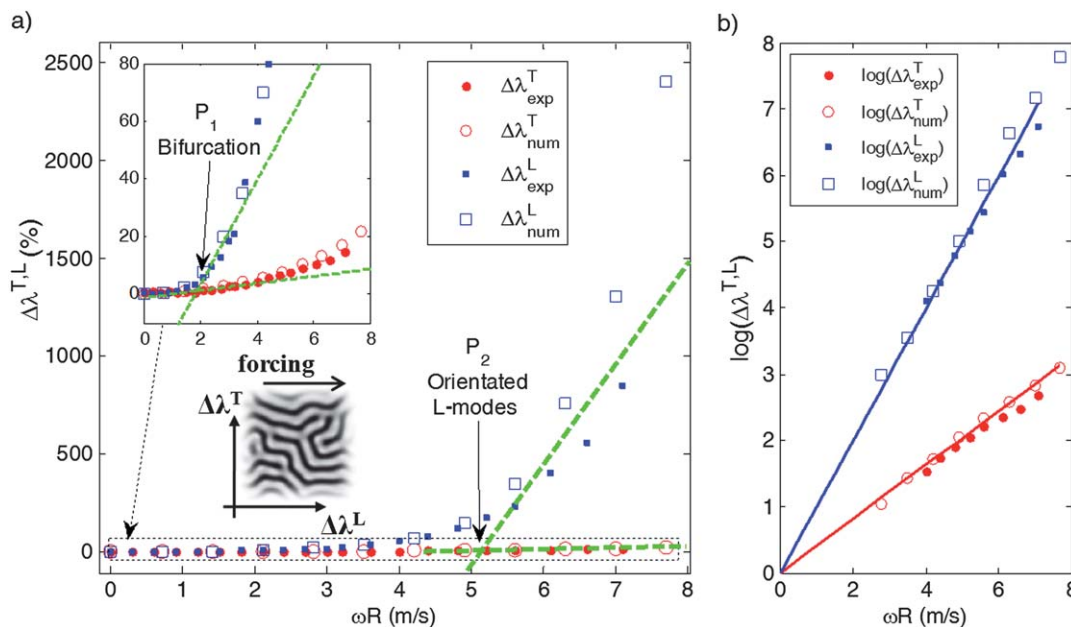


Fig. 6 Representation of the L and T-length mode increment depending on the force. The increments $\Delta\lambda^{L,T}$ are calculated with respect to the wavelength of the standard pattern (λ_0), analogous to Fig. 5. Circles (squares) and red (blue) color stand for transversal (longitudinal) mode. Filled (empty) markers correspond to experimental (numerical) results. (a) Characterization of different orientation regimes versus applied force. Point P_1 marks the first divergence between the L-mode and T-mode and corresponds to the transition state (transition between region I and II). This can be more clearly seen in the inset of the figure. Point P_2 marks the transition between regions II and III. (b) Semilog plot of the same results ($\log(\Delta\lambda^{L,T}) = a_{L,T} \omega R$ with $a_L = 1.02 \pm 0.16$ and $a_T = 0.42 \pm 0.09$).

augments with the force. Experimentally, increments of up to 18% were reported while theoretically and numerically any increment can be achieved up to the inhibition of the Turing pattern (Fig. 3). In this sense, the experimentally encapsulated BZ–AOT reactions are quite robust to a rotational force, and therefore Turing patterns are only moderately modified. Similar effects on the Turing patterns were observed in systems where temperature or concentrations modify the diffusivity.^{36,37}

In addition to the changes in the wavelength, we quantify the orientation of the pattern with respect to the centrifugal forces. From the numerical and experimental data shown in Fig. 2 we calculate the mean separation between stripes in the direction of the force ($\Delta\lambda^L$), and in the transversal direction ($\Delta\lambda^T$), denoted as the longitudinal (L) and transversal (T) wavelength modes, respectively (the definition of these normalized quantities is equivalent to that in Fig. 5). The T-modes are related to pattern wavelength and L-modes take into account the pattern orientation. According to this, patterns in the absence of force (Fig. 2a and d) have similar values for both L and T-modes since there is no preferential direction. The relative wavelength increments, $\Delta\lambda^{L,T}$, for the two modes are shown in Fig. 6. Note that both experimental data and numerically data fit reasonably well onto the same curve.

Fig. 6a shows that above $\omega R = 5 \text{ m s}^{-1}$ (P_2 in the figure) the L-modes experience an important increment because stripes become largely oriented. At the bifurcation point P_1 ($\omega R = 2 \text{ m s}^{-1}$), the L and T-modes first separate from each other. Thus, the interval of force between P_1 and P_2 (from 2 to 5 m s^{-1}) defines a transition zone where the orientation phenomenon begins to evolve. P_1 and P_2 were calculated by intersecting the best correlated linear fits of both modes (see Fig. 6). Note that the points P_1 and P_2 coincide with the transition from stage I to II and from II to III, respectively (see Fig. 2 and 4).

The growth of the L and T-modes can be characterized by a semilog function ($\log(\Delta\lambda^{L,T}) = a_{L,T}\omega R$) (see Fig. 6b). We find that the growth of $\Delta\lambda^{L,T}$ follows exponential laws whose exponents for the L and T modes are $a_L = 1.02 \pm 0.16$ and $a_T = 0.42 \pm 0.09$. According to this, the longitudinal modes have a rate of growth twice as high as the translational mode. In order to maximize the correlation coefficient of the fit, low force points were neglected due to their logarithmic dispersion.

Conclusions

We studied the effect of an external rotational force on the Turing instability. The force modifies the diffusion dynamics at the microscopic scale due to coupling of the pattern formation and the centrifugal force. An estimation of the external force states that it is about a 10% of the thermal energy ($m_1\omega^2 R^2 \sim 0.1 k_B T$).

Nevertheless, their effects have a crucial role in the pattern formation mechanism. This may seem counterintuitive at first sight. Nevertheless, we have to consider that this is a highly non-linear phenomenon where small disturbances may be reflected in a dramatic change in the macroscopic properties of the system. In our present case, this small perturbation destroys the isotropy of the system that it is translated into a non-

isotropic diffusion coefficient that induces the reported changes. A theoretical model for the anisotropic diffusion process was developed, neglecting convective flows due to boundary constraints. We show, both experimentally and numerically, that the anisotropic (inhomogeneous) force has various important effects on the pattern organization. The force changes the pattern from a labyrinth configuration to stripes oriented in the direction of the centrifugal forces. Moreover, a numerical study reveals that for increasing angular velocity, the patterns exhibit a clear radial orientation before passing through an intermediate black-spots configuration and, finally, are inhibited. In order to clarify these transitions, phase diagrams for the experimental and the numerical case were calculated as shown in Fig. 2e and 4e, respectively. A posterior stability analysis of the reaction–diffusion equations indicates that the force is also able to augment the pattern wavelength and completely inhibit the formation of Turing structures. We also observed an increment in the wavelength with the force experimentally and numerically, see Fig. 5. The numerical and the experimental results are in good agreement. Furthermore, the effect of the centrifugal force on the directionality of the patterns has been quantified by comparing the transversal and longitudinal wavelength modes (see Fig. 6).

Previous work²² showed that it was possible to modify the diffusive regime homogeneously; here we present a mechanism capable of introducing anisotropies in the system. The coupling between the perturbations and the pattern development allows us to control the type of final structure. In this regard, the authors want to remark that the present work contributes to obtaining a better understanding of the effects that microscopic flows produce on Turing pattern formation. These mechanisms might be extended to other systems that involve self-organization phenomena. Further, this study also constitutes a straightforward method to introduce anisotropy in a system by simply applying an external field without actually altering the nature of the system.

Acknowledgements

The authors thank Dr. P. Taboada for helpful discussions. This work was supported by the Ministerio de Educación y Ciencia and Xunta de Galicia under Research Grants no. FIS2010-21023 and no. CN2012/315. J.C.-L. and A.v.K. were supported by the MICINN under a FPI and FPU (AP-2009-0713), respectively and J.G.-S. by the Xunta de Galicia under a Predoctoral Grant.

Notes and references

- 1 J. Tabony, *Biol. Cell*, 2006, **98**, 589.
- 2 N. Rashevsky, *Bull. Math. Biophys.*, 1940, **2**, 15.
- 3 I. Prigogine and G. Nicolis, *Q. Rev. Biophys.*, 1971, **4**, 107.
- 4 A. M. Turing, *Philos. Trans. R. Soc., B*, 1952, **237**, 37.
- 5 S. Setayeshgar and M. C. Cross, *Phys. Rev. E: Stat. Phys., Plasmas, Fluids, Relat. Interdiscip. Top.*, 1998, **58**(4), 4485.
- 6 J. M. W. Slack, *From Egg to Embryo. Determinative Events in Early Development*, Cambridge University Press, 1983.

- 7 J. D. Murray, *Mathematical Biology*, Springer, Berlin, 2nd edn, 1993; P. A. Lawrence, *The Making of a Fly: The Genetics of Animal Design*, Blackwell Scientific Publications, Boston, 1992.
- 8 S. Kondo and R. Asai, *Nature*, 1995, **376**, 765.
- 9 H. Meinhardt, *The Algorithmic Beauty of Sea Shells*, Springer, Berlin, 1995.
- 10 D. A. Vasquez and C. Lengacher, *Phys. Rev. E: Stat. Phys., Plasmas, Fluids, Relat. Interdiscip. Top.*, 1998, **58**, 6865.
- 11 I. P. Nagy and J. A. Pojman, *J. Phys. Chem.*, 1993, **97**, 3443.
- 12 J. Carballido-Landeira, V. K. Vanag and I. R. Epstein, *Phys. Chem. Chem. Phys.*, 2010, **12**, 3656.
- 13 S. Rüdiger, D. G. Míguez, A. P. Muñuzuri, F. Sagués and J. Casademunt, *Phys. Rev. Lett.*, 2003, **90**, 128301.
- 14 G. Fernández-García, D. I. Roncaglia, V. Pérez-Villar, A. P. Muñuzuri and V. Pérez Muñuzuri, *Phys. Rev. E: Stat. Phys., Plasmas, Fluids, Relat. Interdiscip. Top.*, 2008, **77**, 026204.
- 15 A. von Kameke, F. Huhn, G. Fernández-García, A. P. Muñuzuri and V. Pérez-Muñuzuri, *Phys. Rev. E: Stat. Phys., Plasmas, Fluids, Relat. Interdiscip. Top.*, 2010, **81**, 066211.
- 16 V. Pérez-Villar, J. L. F. Porteiro and A. P. Muñuzuri, *Phys. Rev. E: Stat. Phys., Plasmas, Fluids, Relat. Interdiscip. Top.*, 2006, **74**, 046203.
- 17 M. Fantz, R. Friedrich, M. Bestehorn and H. Haken, *Phys. D*, 1992, **61**, 147.
- 18 A. P. J. Breu, C. A. Kruelle and I. Rehberg, *Europhys. Lett.*, 2003, **62**, 491.
- 19 V. K. Vanag and D. V. Boulanov, *J. Phys. Chem.*, 1994, **98**, 1449.
- 20 A. N. Zaikin and A. M. Zhabotinsky, *Nature*, 1970, **225**, 535.
- 21 T. K. De and A. Maitra, *Adv. Colloid Interface Sci.*, 1995, **59**, 95.
- 22 J. Guiu-Souto, J. Carballido-Landeira, V. Pérez-Villar and A. P. Muñuzuri, *Phys. Rev. E: Stat. Phys., Plasmas, Fluids, Relat. Interdiscip. Top.*, 2010, **82**, 066209.
- 23 V. K. Vanag, *Phys.-Usp.*, 2004, **47**, 923; V. K. Vanag and I. R. Epstein, *Phys. Rev. Lett.*, 2001, **87**, 228301.
- 24 V. K. Vanag and I. R. Epstein, *Phys. Rev. Lett.*, 2003, **90**, 098301.
- 25 I. R. Epstein and V. K. Vanag, *Chaos*, 2005, **15**, 047510.
- 26 A. Kaminaga, V. K. Vanag and I. R. Epstein, *J. Chem. Phys.*, 2005, **122**, 174706.
- 27 L. Gyorgyi, T. Turanyi and R. J. Field, *J. Phys. Chem.*, 1990, **94**, 7162.
- 28 A. Kaminaga, V. K. Vanag and I. R. Epstein, *Angew. Chem., Int. Ed.*, 2006, **118**, 3159.
- 29 F. A. William, *Numerical Methods for Partial Differential Equations*, Academic Press, New York, 1977.
- 30 D. G. Míguez and A. P. Muñuzuri, *Biophys. Chem.*, 2006, **124**, 161.
- 31 J. Guiu-Souto, J. Carballido-Landeira and A. P. Muñuzuri, *J. Phys.: Conf. Ser.*, 2011, **296**, 012016.
- 32 J. Guiu-Souto, J. Carballido-Landeira and A. P. Muñuzuri, *Phys. Rev. E: Stat. Phys., Plasmas, Fluids, Relat. Interdiscip. Top.*, 2012, **85**, 056205.
- 33 I. M. Cohen and P. K. Kundu, *Fluid Mechanics*, Academic Press, San Diego, 1990.
- 34 K. Huang, *Statistical Mechanics*, John Wiley & Sons, Massachusetts, 1987.
- 35 S. H. Strogatz, *Nonlinear Dynamics and Chaos: With Applications to Physics, Biology, Chemistry, and Engineering*, Westview Press, 1994.
- 36 O. Ouyang, R. Li, G. Li and H. L. Swinney, *J. Chem. Phys.*, 1995, **102**, 2551.
- 37 R. McIlwaine, V. K. Vanag and I. R. Epstein, *Phys. Chem. Chem. Phys.*, 2009, **11**, 1581.